Journal of Energy Storage 144 (2026) 119844

Contents lists available at ScienceDirect

Journal of Energy Storage

journal homepage: www.elsevier.com/locate/est

Research papers

Design and development of heat pipe cooling systems for air & watertight Portable Energy Storage units

Alireza E. Majd [a,*], Collins E. Obazee [b], David S. Adebayo [c], Armin R. Darvazi [d], Nduka N. Ekere [a], Fideline Tchuenbou-Magaia [b,*], Jin Wang [a]

[a] *Faculty of Engineering and Technology, Liverpool John Moores University, Liverpool, UK*
[b] *School of Engineering, Computing and Mathematical Sciences, University of Wolverhampton, Wolverhampton, UK*
[c] *College of Engineering and Physical Sciences, School of Engineering & Technology, Aston University, Birmingham, UK*
[d] *Faculty of Technology and Engineering, University of Guilan, Rasht, Iran*

ARTICLE INFO

Keywords:
Portable Energy Storage (PES)
Thermal management
Heat pipe cooling system
Air & watertight enclosure
Free and forced convections

ABSTRACT

Portable Energy Storage (PES) units play a vital role in delivering reliable and sustainable energy solutions, particularly in regions with limited grid access or challenging environmental conditions that require special Ingress Protection (IP) considerations, such as air and watertight designs without vents. Thermal management is a critical challenge for such PES units, especially for key components such as inverters and battery packages, which are prone to overheating. This study explores the integration of heat pipe-based cooling systems with heatsinks as an effective thermal management solution. A 1-kW PES was designed, developed and assessed as a case study under varying ambient temperatures and operational scenarios. Both free and forced convection cooling methods were evaluated through experiments and validated simulations. Results show that under free convection at an ambient temperature of 23 °C, Metal-Oxide-Semiconductor Field-Effect Transistors (MOSFETs) remained below 70 °C, while Lithium-ion Batteries (LIBs) stabilized at 60 °C. Forced convection with 1.4 W fans significantly improved cooling efficiency, reducing temperatures by 25–45 %, depending on ambient conditions. At 23 °C, a 33 % temperature reduction was observed in both MOSFETs and LIBs. At an ambient temperature of 50 °C, MOSFETs were maintained at 70 °C, and LIBs remained below 60 °C for ambient temperatures up to 45 °C. These findings confirm that heat pipe cooling systems, combined with forced convection, offer an effective thermal management solution for compact, air and watertight PES applications.

1. Introduction

The increasing use of electronic devices and the shift towards sustainable energy systems have led to a growing need for Portable Energy Storage (PES) units that can function reliably across various environmental conditions. PES units, especially those using solid-state batteries, present an efficient and sustainable energy solution, particularly for regions with limited or no access to the grid. However, maintaining thermal stability in high-temperature and dusty environments presents significant challenges for these systems [1,2]. Additionally, the use of watertight enclosures can further enhance the applicability of PES units in high-moisture, rainy conditions, or sea-based applications, ensuring reliable operation in demanding environments.

1.1. Portable Energy Storage (PES) systems

A PES system typically consists of several key components, including solid-state batteries, power inverters, and cooling systems. These units are especially critical in areas with limited grid access, providing off-grid energy through renewable sources like solar photovoltaics. Yet, high-energy-density batteries, such as lithium-ion batteries (LIBs), tend to generate considerable heat during operation, especially in high-power scenarios [3–5]. This overheating can negatively affect battery performance, shorten their lifespan, and, in more extreme cases, lead to safety concerns such as thermal runaway [6]. To mitigate these risks, efficient cooling systems are essential to maintain the optimal operating temperature, which for LIBs is typically between 25 °C and 50 °C, principally when used in airtight designs [7].

Thermal management in PES units is further complicated by the

---

* Corresponding authors.
E-mail addresses: a.eslamimajd@ljmu.ac.uk (A. E. Majd), c.e.obazee@wlv.ac.uk (C.E. Obazee), d.adebayo@aston.ac.uk (D.S. Adebayo), Armrah@guilan.ac.ir (A. R. Darvazi), n.n.ekere@ljmu.ac.uk (N.N. Ekere), f.tchuenbou-magaia@wlv.ac.uk (F. Tchuenbou-Magaia), j.wang@ljmu.ac.uk (J. Wang).

https://doi.org/10.1016/j.est.2025.119844
Received 7 April 2025; Received in revised form 21 October 2025; Accepted 10 December 2025

Nomenclature

Acronyms

AC	Alternating Current
DC	Direct Current
HP	Heat Pipe
LIB	Lithium-Ion Battery
DC	Direct Current
IP	Ingress Protection
MOSFET	Metal-Oxide-Semiconductor Field-Effect Transistor
PES	Portable Energy Storage
PCB	Printed Circuit Board

Symbols

g	Acceleration due to gravity
T_∞	Ambient temperature
L	Characteristic length
A	Cross-sectional area
μ	Dynamic viscosity
K_{eff}	Effective thermal conductivity of heat pipe
Q	Heat flow rate
h	Heat transfer coefficient
H	Height
ν	Kinematic viscosity
m	Mass
N_u	Nusselt number
R_a	Rayleigh number
C_p	Specific heat at constant pressure
T_s	Surface temperature
T	Temperature
ΔT	Temperature difference
K, TC	Thermal conductivity
t	Time
V	Volume
W	Width

demand for compact, lightweight designs factors that are particularly important when space and weight are at a premium [8]. The inclusion of high-power components such as DC-to-AC inverters alongside solid-state batteries creates a significant heat load within the system. For instance, around 10 % of the power in conventional inverters is typically lost as heat, adding complexity to the thermal design [9]. Moreover, traditional active cooling methods like fans and vents are unsuitable for airtight PES units, especially in dusty environments where these systems become impractical or unreliable.

1.2. *Heat pipe technology*

Heat pipes have emerged as an effective solution for passive heat transfer, utilizing the phase change of a working fluid to move heat from a hot area (the evaporator) to a cooler one (the condenser). Commonly used in electronic cooling systems, heat pipes offer excellent thermal conductivity (TC), are lightweight, and operate without requiring external power [10]. The process involves the working fluid evaporating at the heat source, condensing at the cooler end, and then returning to the evaporator through capillary action in a wick structure [11].

The performance of heat pipes is influenced by several factors, including the type of working fluid, the heat pipe configuration, and the design of the wick structure. Water is often the fluid of choice due to its high TC and broad operating range, although other fluids such as acetone and methanol may be used depending on the specific application [12]. Various designs of heat pipes have shown great potential for use in high-power applications. For example, conventional heat pipes with wick structures can successfully dissipated up to 400 W of heat in lithium-ion battery modules [13]. Additionally, heat pipes are especially well-suited to high-temperature environments and compact systems, making them ideal for power electronic applications, including LIBs [8,14]. In addition to PES units, such cooling solutions are also suitable for other high-power electronic device such as Light Emitting Diodes (LEDs), especially in remote or off-grid environments where renewable energy sources like solar PV play a key role in sustaining energy demands [15,16].

Heat pipes not only provide high TC but also eliminate the need for active cooling components. Their ability to maintain performance in dusty, high-temperature conditions enhances the reliability of PES units in harsh environments, such as those found in North Africa [17]. The compactness and lightweight nature of heat pipes, combined with their thermal resistance ranging from as low as 0.04 °C/W to a moderate 0.85 °C/W, highlight their suitability for integration into PES units, where space constraints and power efficiency are critical considerations [10].

1.3. *Original contribution*

This study, is built upon the existing concept by simulating a heat pipe-based passive cooling system for air and watertight PES packages, validated through experimental data from a case study. The objective is to optimize the design for enhanced cooling efficiency and long-term reliability, aligning with IP (Ingress Protection) standards. The design specifically targets ratings, such as IP65 (protection against dust and water jets) and IP67 (protection against dust and temporary submersion in water) to ensure robust performance in challenging environments, including high temperatures, dusty conditions, high moisture levels, heavy rainy weather, and sea-based applications. These IP65/IP67-rated PES designs effectively address challenges across a wide range of applications, such as marine environments, where water ingress is a concern, and scenarios requiring protection from dust, debris, and extreme weather conditions, including residential, commercial, and industrial use cases.

2. Experiment

The experimental setup utilized a heater (a wound wire resistor made of copper) powered by a DC power supply. Prior to the main test, the resistor was individually used and powered with 12.5 W. This value was determined through multiple trials to maintain the surface temperature near 100 °C, a conservative threshold based on literature findings which indicate that while power MOSFETs can operate at junction temperatures up to around 200 °C [18,19], thermal behaviour begins to shift significantly and reliability concerns arise around 100 °C, particularly regarding gate oxide degradation and long-term device performance [19].

A flat aluminium heat pipe (MHP-2550A300A, manufactured by AMEC THERMA-SOL), with dimension of 300 mm in length, 50 mm in width, and 2.5 mm in thickness, and with a grooved wick structure and acetone as the working fluid [20] was used in the experimental setup. One end of the heat pipe was connected to a resistor (serving as the heat source), while the opposite end was attached to an aluminium heatsink, functioning as the condenser. To ensure efficient thermal transfer, all adjacent components were bonded using a high-conductive thermal adhesive pad, which provided seamless contact, and an effective thermal pathway between the interfaced components. The room temperature during the experiment was maintained at approximately 23 °C, and temperature readings were recorded at 2-minute intervals over a stable temperature up to 60 min of operation using both digital thermometers and a thermal camera, Testo 883, made by Testo [21]. The camera's internal shutter provides automatic self-calibration, and its readings were cross-checked with thermometers for accuracy. Table 1 outlines the key specifications and technical details of the items employed for the testing.

2.1. *Test design*

Two types of experiments were conducted to evaluate the cooling performance under free convection (Test 1) and forced convection (Test 2) conditions. For forced convection tests, a 12 V, 1.4 W cooling fan (dimensions: 40 mm × 40 mm × 20 mm, airflow capacity: 7.85 CFM) was used as an auxiliary cooling system attached to the heatsink.

The configuration labels follow a naming convention where the letter and first number (e.g., A1, B2, C1) represent the physical structure and pipe orientation, and the second number indicates the type of cooling condition applied: '1' denotes free convection, and '2' denotes forced convection using the cooling fan. Tests 1 and 2 were carried out for the following three configurations:

- Configuration A1-2: Heat pipe without a bend and without an enclosure.
- Configuration B2-2: Heat pipe with a 90-degree bend and without an enclosure.
- Configuration C1-2: Heat pipe with a 90-degree bend placed inside an aluminium enclosure with dimensions of 100 mm (width) × 220 mm (height) × 250 mm (length) and a thickness of 0.5 mm

Fig. 1 shows the experimental configurations for tests A2, B2, and C2, representing the forced convection tests with the fan installed. For free convection tests (tests A1, B1, and C1), the setups were identical to those shown in Fig. 1, except that the fan was removed from the heatsink. The 1 index in the test name (e.g., A1) refers to free convection conditions, while the 2 index (e.g., A2) refers to forced convection conditions.

2.2. *Heat pipe thermal conductivity*

The effective thermal conductivity (K_{eff}) of the heat pipe was determined using Eq. (1) [22].

$$K_{eff} = \frac{Q \cdot L_{eff}}{A \cdot \Delta T} \tag{1}$$

where Q is the heat load in watts, A is the cross-sectional area of the heat pipe (0.000125 m^2), ΔT is the temperature difference between the evaporator and condenser sections in degree Celsius, and L_{eff} is the effective length in metre, and is expressed by Eq. (2).

Table 1

The main specification and physical dimensions of the components used in the experiments.

Item	Dimensions (mm) and material	Technical specifications
Heatsink	L, H, W: 75, 15, 100 Bulk thickness = 4 Material: Aluminium (Al).	Surface: black anodised. Thermal resistance: 3.4–1.9 °C/W.
Heat pipe	Thickness: 2.5 L, W: 300, 50 Weight: 61 g Material: Al 1070.	Wick structure: Groove Working fluid: Acetone Operating inclination: 0–90° Thermal resistance: < 0.2 °C/W
Resistor	L, H, W: 65, 47, 24.1 Material: Copper	Resistance: 33 Ω. Power rating: 100 W.
Thermal pad	Thickness: 0.25 Material: Acrylic, Fibreglass.	Thermal conductivity: 0.95 W/m. °C. Thermal impedance: 1.8 °C/W.

Note: L = Length (mm); H = Height (mm); W = Width (mm).

$$L_{eff} = \frac{L_{evp} + L_{cod}}{2} + L_{adc} \tag{2}$$

where L_{evp}, L_{cod}, and L_{adc} represent the length of the evaporation, condensation and adiabatic sections of the heat pipe, respectively. The lengths of the different sections of the heat pipe were defined based on the test configuration. L_{evp}, which is the portion of the heat pipe interfaced with the heater, measured to be 65 mm. L_{cod}, interfaced with the heatsink, had a length of 75 mm. L_{adc}, which spans the heater and heatsink, measured to be 160 mm. Using these values and applying Eq. (2), L_{eff} was calculated to be 230 mm.

To ensure consistency in temperature measurements, readings were taken after 10 and 20 min of operation for each configuration (Tests A1–C2) under both free and forced convection conditions. The temperature difference (ΔT) between the evaporator and condenser sections was recorded for each case, as detailed in Table 2. The average ΔT across all six tests was 9.1 °C, with a deviation of less than 3 %. This average value was then applied to Eq. (1), along with a heat load (Q) of 12.5 W and a heat pipe cross-sectional area of 0.000125 m^2, yielding an effective thermal conductivity (K_{eff}) of 2537 $Wm^{-1}K^{-1}$ for the flat heat pipe.

2.3. *Test results*

Fig. 2 presents the temperature distribution captured from the tests using thermal camera after 20 min of operation at stable conditions. The experimental results showed that the maximum temperatures in the resistor for Test A1 and Test B1 were 57.0 °C and 56.3 °C, respectively, while for Test A2 and Test B2, they were 43.5 °C and 42.9 °C, respectively. These results indicate that the 90-degree bend in the heat pipe did not significantly affect its thermal performance, as both configurations effectively transferred heat from the resistor to the heatsink. The results from Test C1 and Test C2 (captured immediately after removing the enclosure's lid) show that the maximum resistor temperatures were 73.7 °C and 55.3 °C, respectively. During Test C2, the temperature was continuously monitored using a digital temperature probe to confirm when the system reached a stable temperature before capturing the thermal image.

Table 2 summarizes the recorded temperatures at the resistor (heat source) for all six test configurations. It also presents the corresponding temperatures at the evaporator and condenser sections, along with the calculated temperature differences (ΔT), which were used to determine the effective thermal conductivity of the heat pipe in Section 2.2.

To assess the reliability of the experimental results, an error analysis was conducted. The thermocouples used had an accuracy of ±1 °C (as specified by the manufacturer), and the data acquisition system had a resolution of 0.1 °C. Sensor positioning was carefully maintained across all tests to minimise deviation, and insulation was used to prevent ambient thermal interference. Each configuration was tested twice, with temperature measurements recorded consistently. The maximum variation in results across repeated tests was within ±3 %, showing the overall uncertainty in the experimental temperature.

A comparison between Test B1 (without enclosure) and Test C1 (with enclosure) indicates that placing the resistor and heat pipe inside the enclosure caused approximately a 30.9 % increase in the resistor temperature, attributed to the elimination of natural convection between the heat pipe and the ambient air. Additionally, a comparison of the maximum resistor temperatures between the free convection tests (A1, B1, and C1) and the forced convection tests (A2, B2, and C2) shows that the introduction of the cooling fan reduced the maximum temperatures by approximately 24 % across each test pair.

3. Simulation

The transient state thermal temperature simulations using Ansys 2024 were conducted and configured according to the experimental

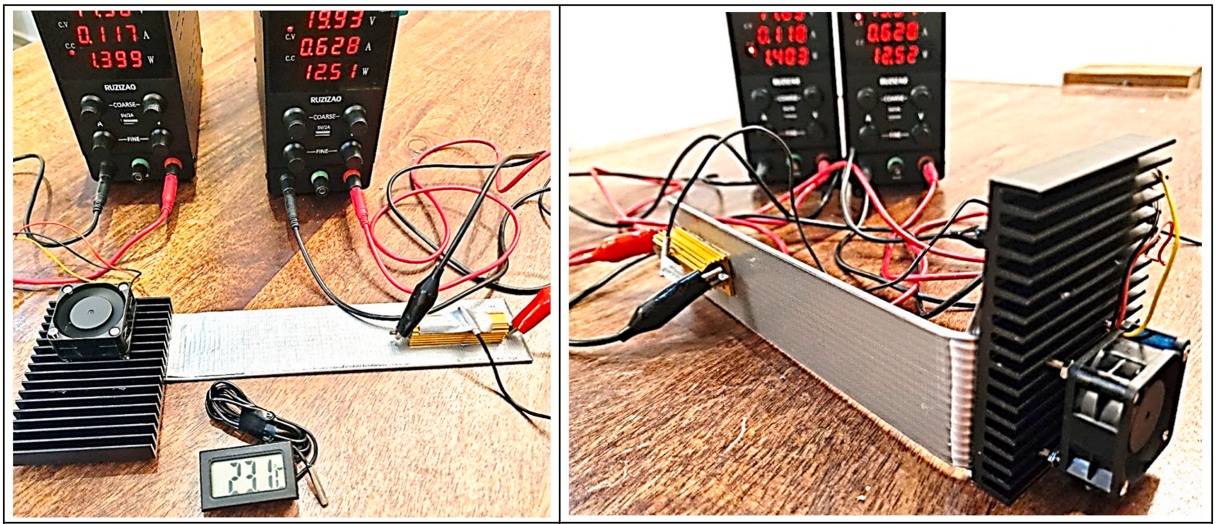

(a) Test A2

(b) Test B2

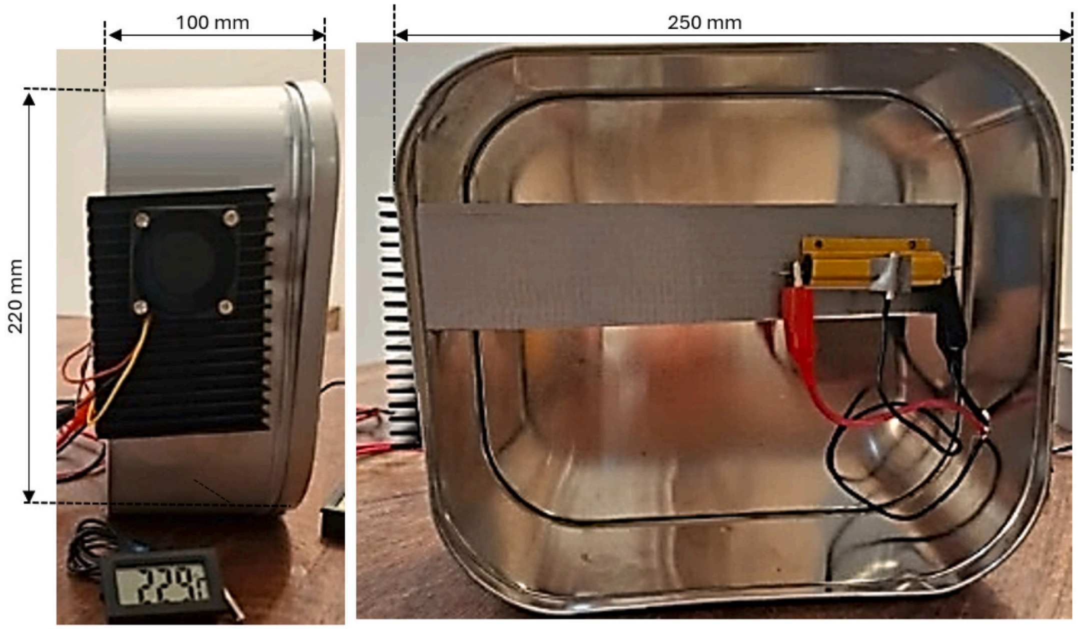

(c) Test C2. Left: side view. Right: front view

Fig. 1. Experimental configurations for Tests A2 and B2 (without enclosure) and Test C2 (with enclosure), displaying side and front views of the setup (showing tested enclosure's dimensions).

Table 2
Experimental temperature measurements and test specification for each configuration showing temperatures at the resistor, evaporator, and condenser sections of the heat pipe, along with the calculated temperature difference between evaporator, and condenser sections (ΔT).

Test	Configuration description	Enclosure	Cooling method	Resistor Temp. (°C)	Evaporator Temp.(°C)	Condenser Temp. (°C)	ΔT (Evap. – Cond.) (°C)
A1	Straight HP	No	Free	57	50.2	41	9.2
A2	Straight HP	No	Forced	43.5	34.9	26.1	8.8
B1	90° Bent HP	No	Free	56.3	46.3	37	9.3
B2	90° Bent HP	No	Forced	42.9	34.2	25	9.2
C1	90° Bent HP	Yes	Free	73.7	62.1	53	9.1
C2	90° Bent HP	Yes	Forced	55.3	45.3	36.5	8.8

setup, accounting for both cases: with and without the aluminium enclosure. The ambient and initial temperature was set at 23 °C and applied uniformly across the system. Heat flow transfer in the system was set to 12.5 W to maintain consistent testing conditions, as established in the experimental setup. For heat generation, the core cylindrical section, with dimensions of 11 mm in diameter and 65 mm in length, within the copper resistor was specified as the heat source with a heat generation rate of 2.02×10^6 Wm^{-3}. Table 3 provides a summary of

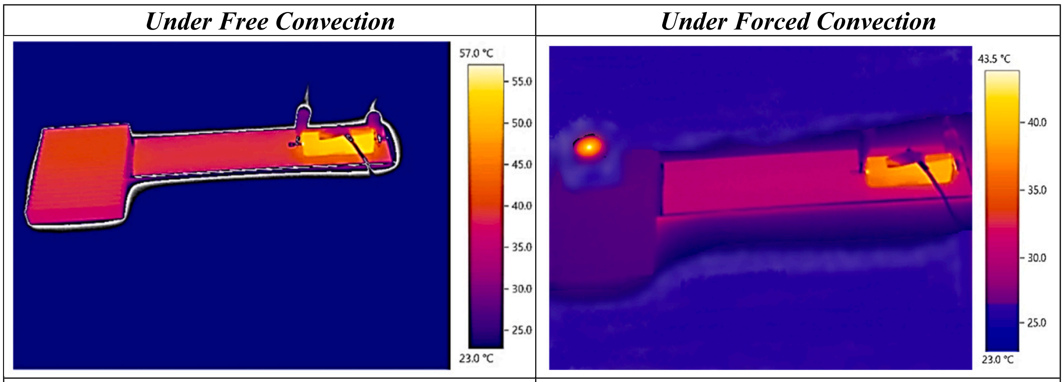

(a) Test A1 (b) Test A2

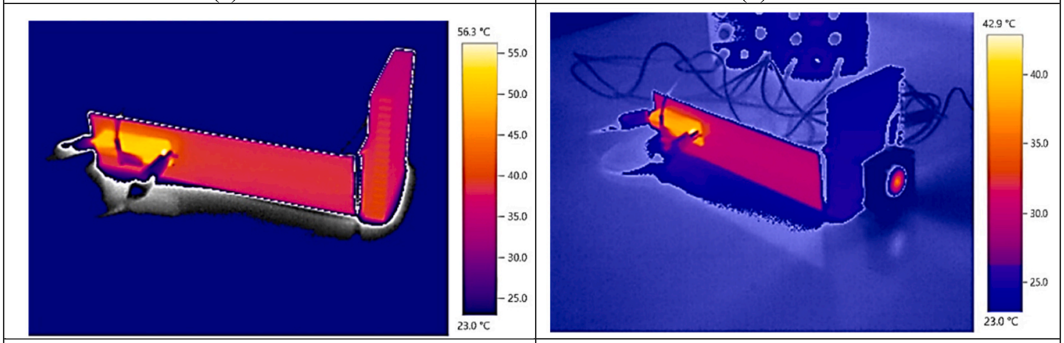

(c) Test B1 (d) Test B2

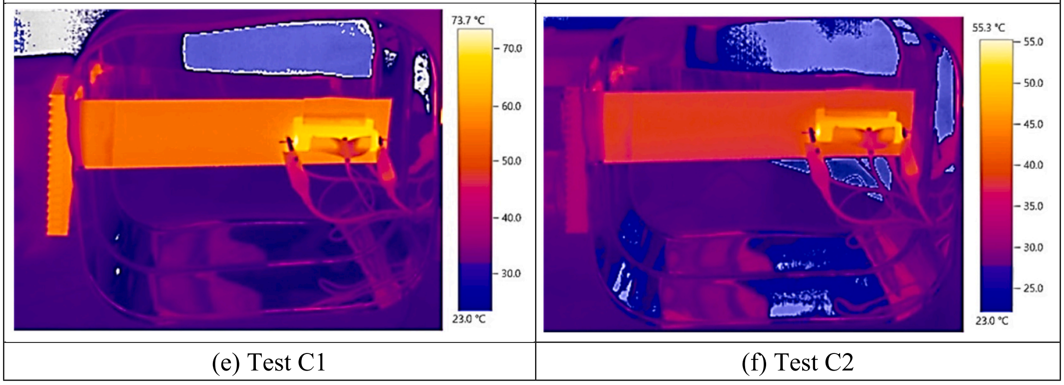

(e) Test C1 (f) Test C2

Fig. 2. Temperature distribution after 20 min operation from experimental tests (captured by Testo thermal camera).

Table 3
General thermal specifications of materials used in the simulation [23].

Component	Parameter	Value	Unit
Copper	Isotropic TC	400	$Wm^{-1}K^{-1}$
	Specific heat capacity	385	$Jkg^{-1}K^{-1}$
	Density	8933	kgm^{-3}
Aluminium	Isotropic TC	237.5	$Wm^{-1}K^{-1}$
	Specific heat capacity	951	$Jkg^{-1}K^{-1}$
	Density	2689	kgm^{-3}
Air	Isotropic TC	0.0242	$Wm^{-1}K^{-1}$
	Specific heat constant pressure	1006.4	$Jkg^{-1}K^{-1}$
	Density	1.225	kgm^{-3}

the material specifications in the simulation.

To ensure the reliability of the simulation results, a comprehensive mesh sensitivity analysis was conducted on all key components, including the resistor, heat pipe, heatsink, air domain, and enclosure plates. Hexahedral (Hex Mapped) elements were used throughout the model to ensure improved mesh quality. Five mesh densities were tested for the solid components (resistor, heat pipe, heatsink): 1 mm, 2 mm, 3 mm, 4 mm, and 6 mm. For instance, in the free convection simulation of the heat pipe with bend configuration (Test B1), the maximum temperature varied between 57.87 °C and 58.8 °C. A mesh size of 2 mm was selected as the optimal balance between computational efficiency and accuracy, with simulation deviation remaining below 1 %.

Similarly, for the air domain and enclosure plates (Test C1), mesh sizes of 1 mm, 2 mm, 4 mm, 6 mm, and 8 mm were evaluated. A 4 mm mesh was chosen using program-controlled scoping, with a minimum edge length of 0.25 mm. The resulting temperature range was approximately 52.1 °C to 53.5 °C, corresponding to a mesh sensitivity error of less than 2 %. The results, including selected mesh sizes, observed temperature ranges, and estimated error margins, are summarized in Table 4.

Also, the transient thermal simulations were carried out with program-controlled solver settings. Auto time stepping was enabled to allow the solver to dynamically adjust the time increments based on convergence behaviour. The initial time step was set to 0.1 s, with a minimum allowable time step of 0.005 s and a maximum time step limit of 3.0 s.

Table 4
Mesh sensitivity results for solid and fluid domains, showing temperature range and error margin.

Component	Mesh sizes tested (mm)	Tolerance range (°C)	Selected mesh	Max Temp (°C)	Approx. error range (%)
Resistor/heat pipe/heatsink	1, 2, 3, 4, 6	57.87–58.8	2 mm	57.95 (Test B1)	<1 %
Air domain/enclosure plates	1, 2, 4, 6, 8	52.1–53.5	4 mm	52.5 (Test C1)	<2 %

3.1. *Free convection*

For Test A1, free convection heat transfer was considered for the external faces of all the components exposed to the ambient air, including the heatsink, resistor hub, and heat pipe. For each component, the convective heat transfer coefficient, h, was calculated for different temperatures (as indicated in Table 5) using Eq. (3) [24].

$$h = \frac{Nu \cdot K}{L} \tag{3}$$

where K is the thermal conductivity of air, and L is the characteristic length of the component and N_u is the Nusselt number defined as follows:

Vertical Plates:

$$N_u = \begin{cases} 0.59\, {R_a}^{\frac{1}{4}}, & 10^4 \le R_a < 10^9 \\ 0.1\, {R_a}^{\frac{1}{3}}, & 10^9 \le R_a < 10^{13} \end{cases} \tag{4-1}$$

Horizontal Plates:

$$N_u = \begin{cases} 0.54\, {R_a}^{\frac{1}{4}}, & 10^4 \le R_a < 10^7 \\ 0.15\, {R_a}^{\frac{1}{3}}, & 10^7 \le R_a < 10^{11} \end{cases} \tag{4-2}$$

where R_a is the Rayleigh number and is defined by Eq. (5).

$$R_a = \frac{2 \cdot g \cdot (T_s - T_\infty) \cdot L^3}{\nu^2 \cdot (T_s + T_\infty)} \cdot \frac{C_p \cdot \mu}{K} \tag{5}$$

where g is gravitational acceleration (9.81 m/s^{-2}), T_s is the surface temperature, T_∞ is the ambient temperature, C_p is the specific heat capacity at constant pressure, K is the thermal conductivity, μ is the dynamic viscosity of air, ν is the kinematics viscosity. The dynamic and kinematic viscosity values of air at atmospheric pressure and temperature at 23 °C were taken as 18.2×10^{-6} Pa.s, and $15.5 \times 10^{-6}\ m^2 s^{-1}$, respectively.

The transient state thermal simulation results under free convection conditions were obtained after performing a mesh sensitivity analysis, ensuring the accuracy of the results once the system reached a stable thermal state. In line with the experimental setup described in Section 2, free convection simulations were conducted to validate the modelling approach for Test A1 and Test B1 (both without enclosure) and Test C1 (with enclosure).

For Test C1, where the heat pipe and resistor were housed inside an aluminium enclosure, internal free convection between the heat pipe, resistor, and surrounding air was eliminated. However, free convection was still applied to the external surfaces of the enclosure, including the side panels (vertically oriented), the top panel (horizontally oriented), and the front and rear panels (vertically oriented), all of which were exposed to the ambient environment. Since the heatsink remained outside the enclosure and directly exposed to ambient air, free convection was also applied to the heatsink surface in Test C1. The corresponding convective heat transfer coefficients (h) applied to these external panels are summarized in Table 5.

For the tests conducted under free convection conditions, Fig. 3 shows the simulated maximum temperatures in the resistor for Test A1, Test B1, and Test C1, which were approximately 58.4 °C, 57.9 °C, and 72.6 °C, respectively. Compared to the corresponding experimental results shown in Fig. 2(a), (c), and (e), these simulations exhibited errors of approximately 2.5 %, 2.8 %, and 1.5 %, respectively. This demonstrates good agreement between the simulation and experimental results, validating the accuracy of the free convection modelling approach.

3.2. *Forced convection*

To study the effect of forced convection on the heatsink, the simulation model based on Test A1 was adapted. The heat transfer coefficient for natural convection was first calculated using standard Nusselt number correlations, as outlined in Section 1. Multiple simulations were conducted by applying varying amplitude factors to the baseline value to simulate forced convection on the heatsink surface. The amplitude factor that successfully reproduced the temperature reduction observed experimentally was found to be 4.75. Using this factor, the simulation yielded a maximum temperature of 42.5 °C (as shown in Fig. 4(a)), which closely matches the experimental result from Test A2 presented in Fig. 2(b).

This identified amplitude factor was then applied to the simulation models for Tests B2 and C2 to cross-validate its effectiveness in different configuration with and without enclosures. Comparing the simulation results from Tests B2 and C2 (shown in Fig. 4(b) and (c), respectively) with the corresponding experimental data shown in Fig. 2(d) and (f), the maximum simulated temperatures were approximately 42.2 °C and 52.5 °C, respectively. These results correspond to simulation errors of

Table 5
Convective heat transfer coefficient (h) for the components used in the simulation.

Components		Small heatsink	Large heatsink	Resistor	Heat pipe	Enclosure side panels	Enclosure top panel	Enclosure front/back panels
Position		Horizontal	Horizontal	Horizontal	Horizontal	Vertical	Vertical	Horizontal
L (m)		0.075	0.2	0.065	0.3	0.25	0.22	0.22
T_s (°C)	$T_s - T_\infty$ (°C)	h ($Wm^{-1}K^{-1}$)						
30	7	3.75	2.93	3.89	2.65	3.03	2.87	3.13
35	12	4.28	3.35	4.44	3.03	3.46	3.27	3.57
40	17	4.66	3.65	4.83	3.30	3.77	3.87	3.89
45	22	4.96	3.88	5.14	3.51	4.01	4.21	4.14
50	27	5.21	4.08	5.40	3.69	4.21	4.49	4.35
55	32	5.43	4.25	5.62	3.84	4.39	4.74	4.53
60	37	5.62	4.40	5.82	3.97	4.54	4.97	4.69
65	42	5.79	4.53	6.00	4.09	4.68	5.17	4.83
70	47	5.94	4.65	6.16	4.20	4.80	5.35	4.96

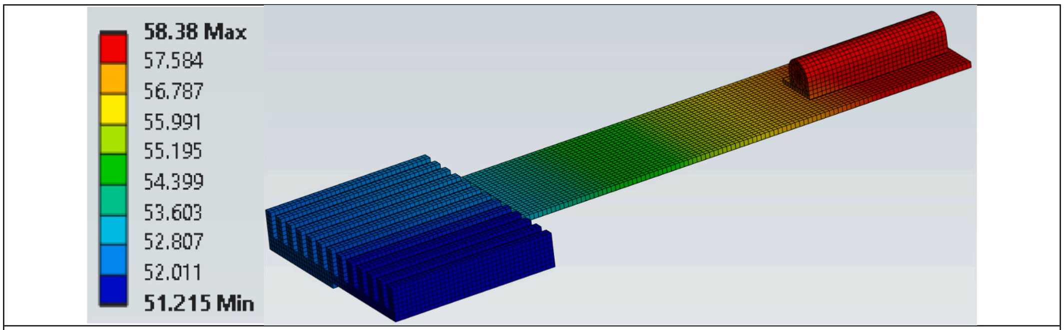

(a) Test A1

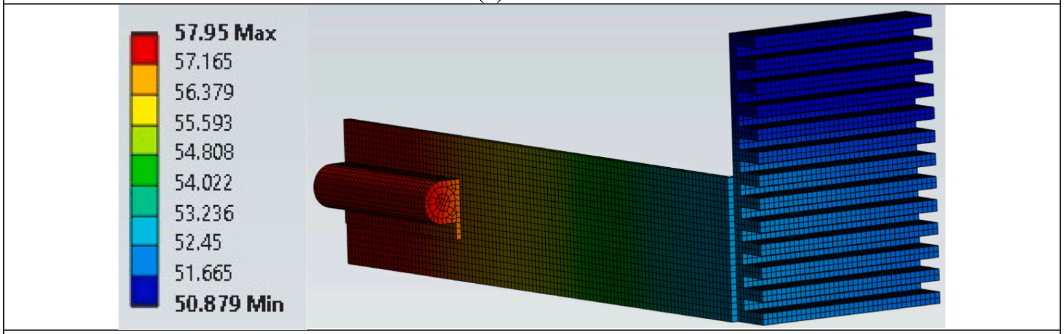

(b) Test B1

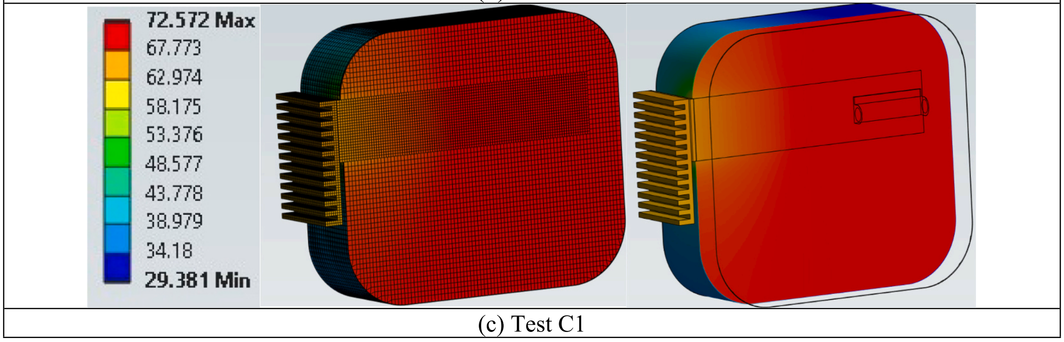

(c) Test C1

Fig. 3. Temperature distribution from simulations under free convection for Test A1 and B1 (without enclosure) and Test C1 (with enclosure; left image shows the mesh display in the mid-section of the enclosure; right image shows the same view without mesh display).

approximately 1.63 % and 5 %, respectively. While this factor is specific to the fan used in this study, the same fan model (12 V, 1.4 W, 7.85 CFM) was employed in all forced convection tests, operating at the same speed and installed in an identical position on the heatsink. Therefore, applying the same amplitude factor across configurations was reasonable.

Table 6 presents a summary of the results comparing the maximum temperatures recorded at the resistor in both experiments and simulations for all six test configurations under the modelled conduction-convection coupling. As can be seen, the relatively low errors confirm the robustness of this simulation strategy for evaluating thermal performance in similar setups.

The heat transfer process in the simulated scenarios is governed primarily by a combination of conductive heat spreading through the aluminium casing and heat pipe, and convective dissipation from the heatsink surface. The thermal gradient along the heat pipe further confirms its active role in transporting heat from the resistor base to the fins, where cooling occurs. Under free convection, buoyancy-driven airflow limits heat removal efficiency, while the forced convection case benefits from higher heat transfer coefficients due to externally imposed airflow, enhancing surface heat removal. This clear reduction in peak component temperatures under forced convection highlights the impact of increased convective heat transfer.

4. Cooling system design for PES

A standard-size PES unit with a 1 kW DC-to-AC inverter was used to assess the performance of a heat pipe cooling system integrated with external heatsinks. The PES package considered to incorporate an enclosure with dimensions of 200 mm (width) × 300 mm (height) × 400 mm (length) and a thickness of 1 mm.

The inverter included eight SiC MOSFETs (thermal conductivity: 320 $Wm^{-1}K^{-1}$ [25]; specific heat capacity: 560 $Jkg^{-1}K^{-1}$ [18]), operating at up to 90 °C with a power loss of 2.2 % [26], resulting in a uniform heat dissipation of 2.75 W per MOSFET.

The PES incorporated a 1 kWh lithium-ion battery (LIB) composed of 18,650 cylindrical cells, generating 40.54 W of heat at a 2.2 A discharge rate. The cells were housed in an aluminium casing (142 × 186 × 138 mm, with wall thickness of 2 mm) in two rows. In the simulation setup, the cylindrical LIBs were arranged in two rows within the aluminium casing, with the heat pipe embedded centrally between alternating cell columns. Ideal thermal contact was assumed between the LIBs, casing, and heat pipe to replicate effective thermal conduction, as illustrated in Fig. 5. Table 7 outlines the main specifications for the proposed LIB as the case study in this work.

Three cooling system configurations incorporating heat pipes integrated with heatsinks were evaluated. Each pair of heat pipes was connected to the inverter's MOSFETs (four on each side) and extended

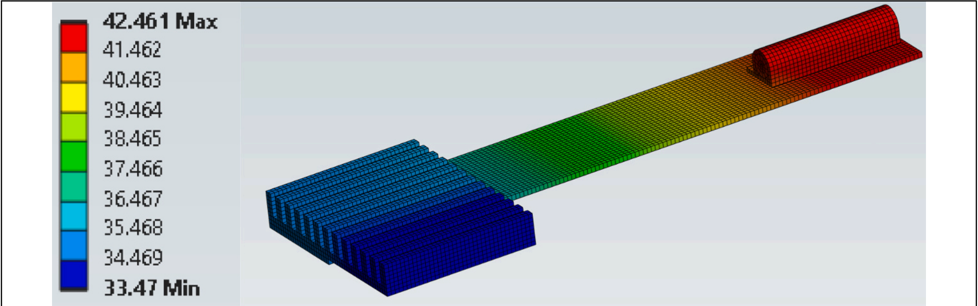

(a) Test A2

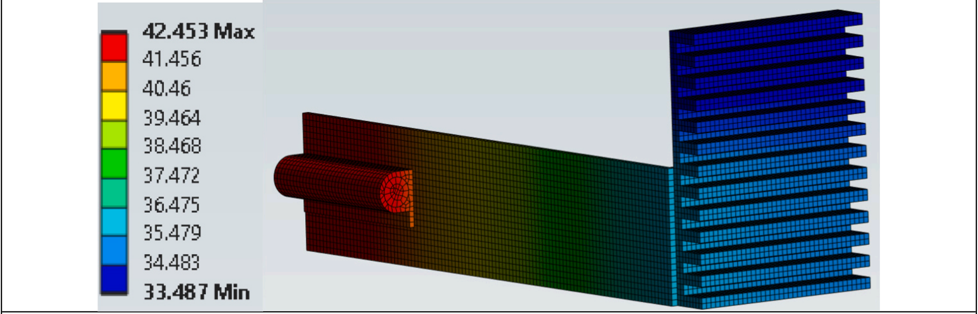

(b) Test B2

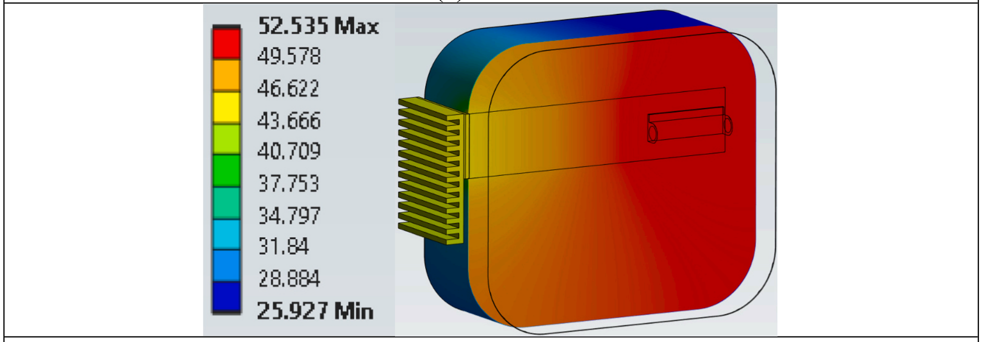

(c) Test C2

Fig. 4. Simulation results for temperature distribution in Tests A2, B2, and C2, demonstrating the effect of forced convection with the amplified convective heat transfer coefficient applied to the heatsink.

Table 6
Summary of the results (maximum resistor temperature (°C)) found through the experiments and simulations, and the corresponding error.

Test	Cooling method	Simulation	Experiment	Corresponding error (%)
A1	Free	58.4	57.0	2.5 %
A2	Forced	42.5	43.5	2.3 %
B1	Free	57.9	56.3	2.8 %
B2	Forced	42.5	42.9	0.9 %
C1	Free	72.6	73.7	1.5 %
C2	Forced	52.5	55.3	5.1 %

through the LIB casing to enhance thermal management, as illustrated in Fig. 5.

- ***Model I:*** *Two heat pipe pairs, one for the inverter and one for the LIBs, each connected to small heatsinks as introduced in the validation section.*
- ***Model II:*** *Similar to Model I, but the small heatsinks were replaced by a* ***large heatsink (200 × 100 mm)*** *with a convective heat transfer coefficient.*
- ***Model III:*** *Same as Model II, but the LIBs used* ***two heat pipe pairs*** *instead of one and a larger* ***heatsink (200 × 140 mm)****.*

The simulations followed the same approach as the validation process using transient thermal analysis in Ansys 2024 to transfer heat at an ambient temperature of 23 °C.

5. Result and discussion

5.1. Free convection for the PES design

As the heatsink was positioned outside the package, free convection conditions were applied. Additionally, free convection was applied to the external surfaces of the PES casing, including the side panels (positioned vertically), the top panel (positioned horizontally), and the front and back panels (positioned vertically), as these surfaces were exposed to ambient air. The convective heat transfer coefficients (h) applied to these panels are listed in Table 3.

Fig. 6 illustrates the temperature distribution in the PES, highlighting the maximum temperatures in the MOSFETs and the battery pack for Models I, II, and III under free convection conditions after 20 min of operation. As observed, the rear side of MOSFETs, which are farthest from the heatsink, consistently exhibit higher temperatures compared to the front side of MOSFETs, which are closer to the heatsink.

Across all three models, the temperatures of the MOSFETs remained below 70 °C, ensuring reliable operation with sufficient safety margins. Additionally, the heatsink temperatures in Models I and II remained consistent at approximately 62 °C, indicating steady thermal dissipation

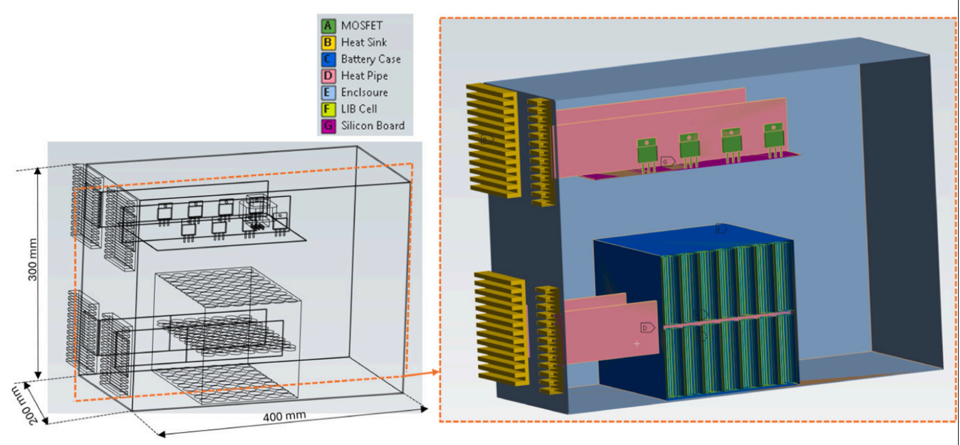

(a) Model I, Left: 3D wireframe view with the dimensions of enclosure. Right: 3D cut-view showing the individual components of the simulated PES.

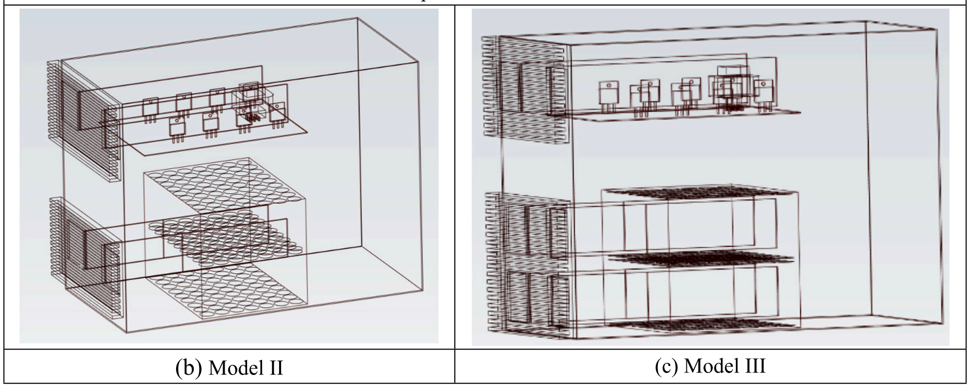

(b) Model II

(c) Model III

Fig. 5. Simulation view of the PES configurations showing the 1 kW inverter and 1 kWh battery pack.

Table 7
Specifications and parameter list of the 18,650 cylindrical LIB [27,28].

Nominal voltage (v)	3.7
Nominal capacity (Ah)	2.2
Cell diameter (mm)	18
Cell height (mm)	65
Cell numbers	126
Power (W)	1025
Heat generation rate (Wm^{-3}) at 2.2 A discharge rate	19,454
Density (kgm^{-3})	2745
Heat specific ($Jkg^{-1}K^{-1}$)	960
Thermal conductivity ($Wm^{-1}K^{-1}$)	160
Discharge temperature (°C)	−20-60

performance.

For Models I and II, the maximum temperatures in the MOSFETs and LIBs are approximately 70 °C and 67.5 °C, respectively, indicating that using two small heatsinks (75 mm × 100 mm) is almost as effective as employing a single large heatsink (100 mm × 200 mm) connected to a pair of heat pipes. Additionally, the temperatures of the heatsinks in both models were approximately 61 °C.

In Model III, the maximum temperature in the LIBs was around 60 °C, representing an approximate 11 % reduction compared to Models I and II. This improvement, achieved by employing two pairs of heat pipes for the LIBs, ensures a safe operating temperature for the battery pack, keeping it well below the safe threshold of 60 °C [28–34].

5.2. Forced convection for the PES design

Fig. 7 presents the temperature distribution in the PES for Model III under forced convection conditions at an ambient temperature of 23 °C, using transient thermal analysis in Ansys 2024. This configuration includes an external 1.4 W cooling fan for each heatsink (considering the modified amplitude factor of 4.75 for the natural convection coefficient) to enhance heat dissipation and improve the system's thermal performance. The results in Fig. 7 indicate that the maximum temperatures in the MOSFETs and LIBs are approximately 45 °C and 39 °C, respectively. A comparison of Model III with and without external fans demonstrates a significant 33 % reduction in temperature within the PES, highlighting the effectiveness of forced convection in improving the cooling efficiency.

5.3. PES configuration Model III under varying ambient temperature conditions

The simulation of the PES configuration Model III under varying ambient temperature conditions, ranging from 10 °C to 50 °C in 5 °C intervals was investigated. The simulations were conducted under different scenarios of heatsinks under free and forced convections and different power delivery rates outlined in Table 8.

5.3.1. PES under free convection

Figs. 8 and 9 present the simulation results for the maximum temperatures in the MOSFETs and LIBs, respectively, across varying ambient temperatures for configuration Model III under Scenarios A, B, and C stated in Table 8. Temperatures were recorded after 20 min of operation, once stable states were reached.

As Fig. 8 illustrates, the maximum temperature of the MOSFETs remains below 90 °C for all studied scenarios when the ambient temperature is under 43 °C. For higher ambient temperatures up to 50 °C, only the case with 1 kW power delivery shows MOSFET temperatures exceeding this limit, reaching up to 96 °C at an ambient temperature of

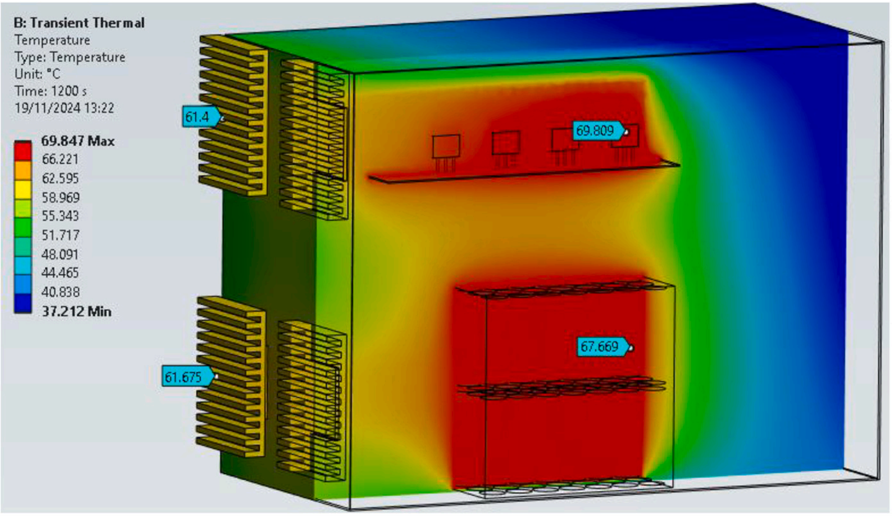

(a) Model I

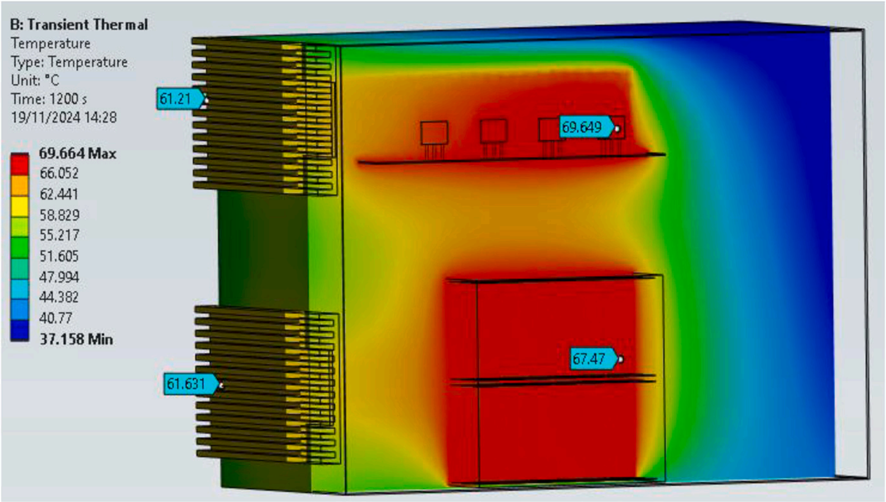

(b) Model II

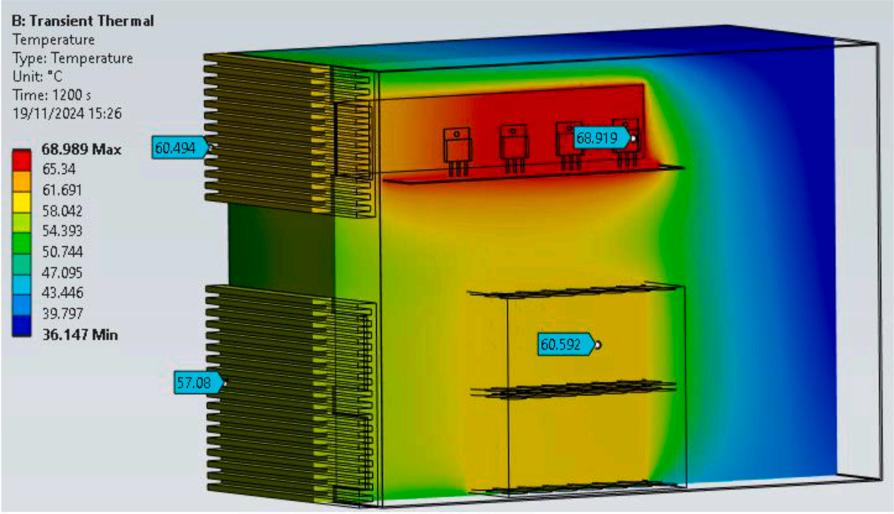

(c) Model III

Fig. 6. Temperatures in the different PES cooling system designs under free convection, showing the max. temp. in the MOSFETs, LIBs, and heatsinks after 20 min operation.

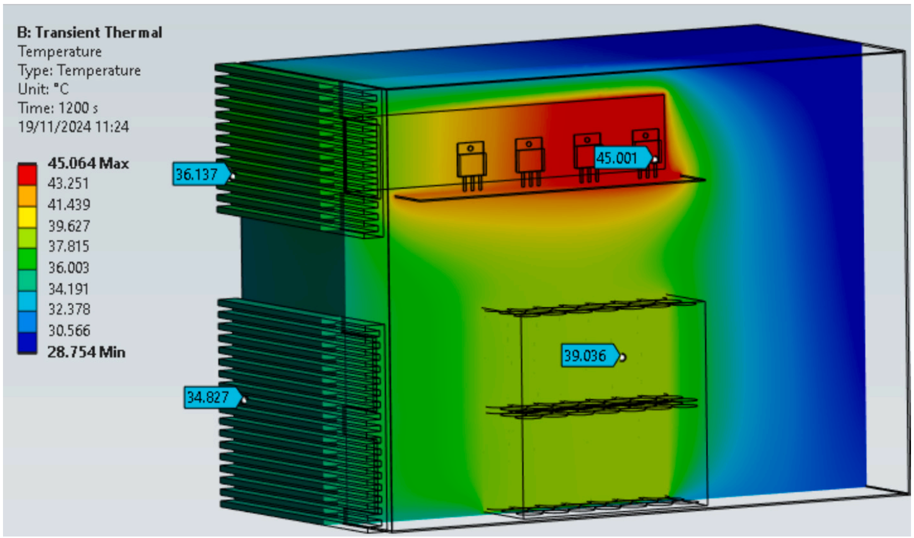

Fig. 7. Temperature distribution in the PES for Model III after 20 min of operation at 23 °C ambient temperature, incorporating heatsinks cooled under forced convection with external 1.4 W fans.

Table 8
Scenarios for Model III simulation.

Scenario	Convection type	PES power delivery	Heat loss
A	Free convection	1 kW	As described in Section 3.1
B		0.7 kW	70 % of Scenario A
C		0.5 kW	50 % of Scenario A
D	Forced convection (with fans)	1 kW	As described in Section 3.2
E		0.7 kW	70 % of Scenario D
F		0.5 kW	50 % of Scenario D

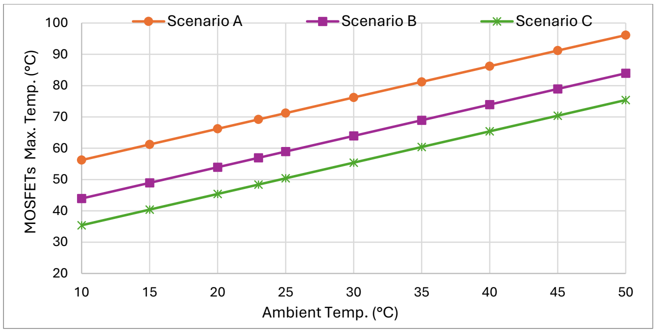

Fig. 8. Simulation results showing the maximum temperatures of MOSFETs for Scenarios A, B, and C across varying ambient temperatures, after 20 min of operation.

50 °C. Despite this, the MOSFETs still operate within a reliable temperature range, although it is preferable to keep their temperatures below 90 °C. Furthermore, the trend of the data in Fig. 8 indicates that at an ambient temperature of 50 °C, reducing the power delivery by approximately 15 % is sufficient to keep the MOSFETs' temperature below 90 °C. This highlights the importance of adjusting power delivery to manage effectively thermal loads in high-temperature environments.

As observed in Fig. 9, the LIBs display a distinct thermal behaviour compared to the MOSFETs. The maximum temperature of the LIBs reaches the critical threshold of 60 °C at an ambient temperature of 23 °C for 1 kW power delivery (Scenario A). At an ambient temperature of 50 °C, the LIBs exhibit significantly higher temperatures, reaching 87 °C under the same power delivery conditions.

At 50 °C ambient temperature but with lower power delivery rates, the LIBs demonstrate improved thermal performance. The maximum temperatures recorded were 77 °C for 0.7 kW power delivery (Scenario B) and 70 °C for 0.5 kW power delivery (Scenario C). Additionally, Fig. 9 indicates that at an ambient temperature of 40 °C, LIBs remain below the critical 60 °C threshold for 0.5 kW power delivery (Scenario C).

Although reducing the power delivery at 40 °C ensures that the LIBs remain under temperature threshold, this solution could involve increasing the size of the battery package for effectively delivering original power delivery, 1 kW, to meet the inverter's maximum capacity and provide the required package power output. The results also highlight the limitations of the current cooling system for the LIBs under free convection of heatsinks at high ambient temperatures, particularly at higher power delivery rates. To address this challenge, forced cooling of the heatsinks using fans could be implemented.

As Figs. 8 and 9 demonstrate, the maximum temperatures in both the MOSFETs and LIBs increase linearly with rising ambient temperatures. However, a nonlinear trend was observed when comparing the recorded maximum temperatures across Scenarios A, B, and C. For instance, reducing the power delivery by 30 %, from 1 kW in Scenario A to 0.7 kW in Scenario B, resulted in a logarithmic decrease in maximum temperatures for both the MOSFETs and LIBs, as illustrated in Fig. 10.

5.3.2. PES under forced convection

Figs. 11 and 12 compare the simulation results for the maximum temperatures in the MOSFETs and LIBs, respectively, across varying ambient temperatures for Model III under different power deliveries in Scenarios D, E, and F.

As shown in Fig. 11, the MOSFETs exhibit a maximum temperature of 70 °C in the most critical case of PES with 1 kW power delivery (Scenario D) at an ambient temperature of 50 °C. This demonstrates the effectiveness of external fans in maintaining the MOSFETs' temperature marginally below the reliable threshold, showcasing excellent thermal performance for the studied PES design.

In Fig. 12, the LIBs maintain maximum temperatures below the threshold of 60 °C for ambient temperatures up to 45 °C, across all power delivery scenarios. Fig. 12 also highlights that under scenario E (0.5 kW power delivery), the LIB maximum temperature remained below 60 °C even at an ambient temperature of 50 °C. However, for scenario F (0.7 kW power delivery), the temperature slightly exceeded the threshold, reaching 61 °C.

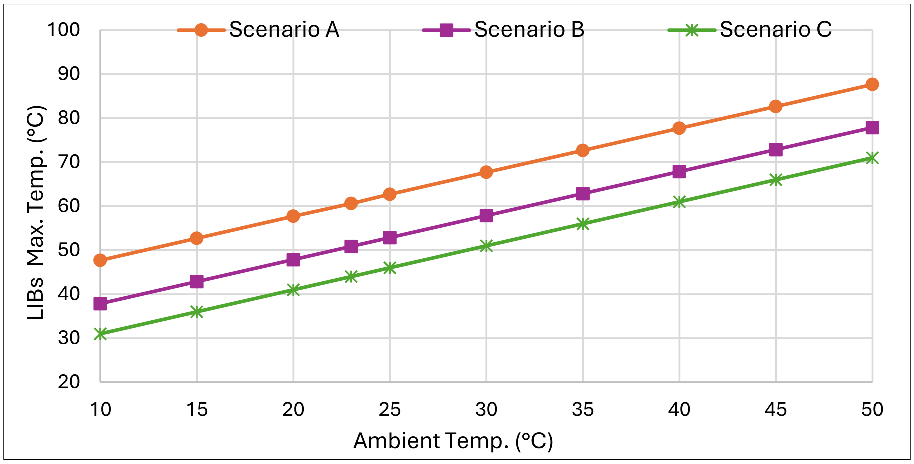

Fig. 9. Simulation results showing the maximum temperatures of LIBs for Scenarios A, B, and C across varying ambient temperatures, after 20 min of operation.

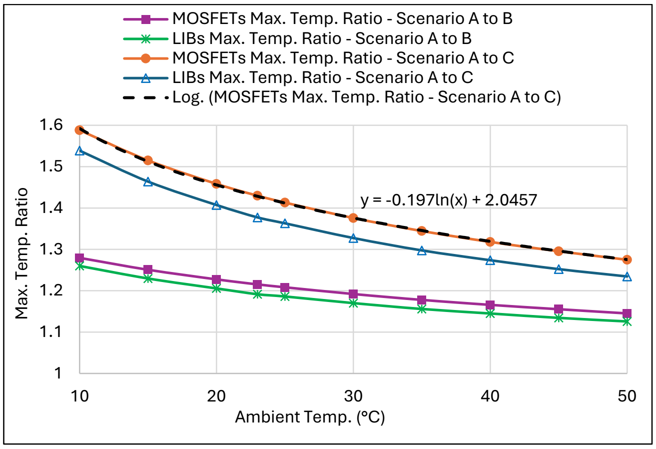

Fig. 10. Simulation results showing the ratio of maximum temperatures in the MOSFETs and LIBs for scenario A to scenario B, and scenario A to scenario C across varying ambient temperatures.

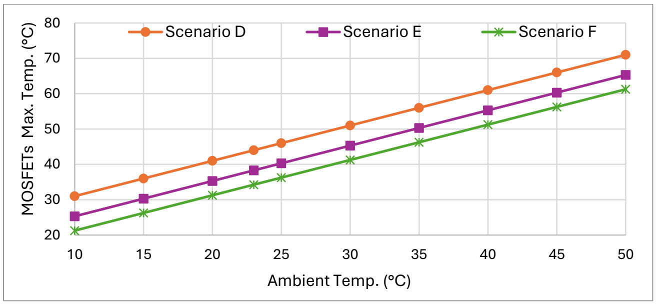

Fig. 11. Simulation results showing the maximum temperatures in the MOSFETs under forced convection at varying ambient temperatures for scenarios D, E, and F.

[Fig. 13](#) illustrates the temperature reductions achieved in the MOSFETs and LIBs under different scenarios when an external fan is used to cool the heatsinks. The results show up to 26 % reduction in the MOSFETs' temperature and 25 % reduction in the LIBs' temperature at an ambient temperature of 50 °C. At lower ambient temperatures, such as 10 °C, the reduction rates increased significantly, with both components exhibiting nearly 45 % temperature reduction compared to cases without external fans. This trend indicates that decreasing the ambient temperature amplifies the effectiveness of forced convection in reducing thermal loads.

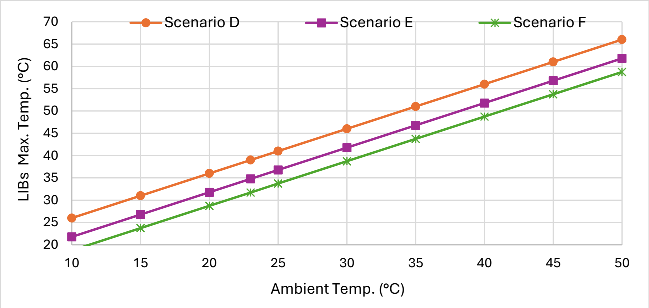

Fig. 12. Simulation results showing the maximum temperatures in the LIBs under forced convection at varying ambient temperatures for scenarios D, E, and F.

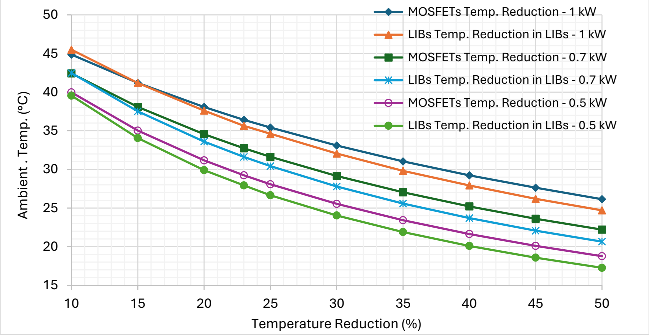

Fig. 13. Temperature reduction in the MOSFETs and LIBs under different power delivery scenarios of the PES, using an external fan for heatsink cooling.

6. Conclusion

Portable Energy Storage (PES) units play a crucial role in delivering reliable and sustainable energy solutions, particularly in regions with limited grid access or challenging environmental conditions such as dusty environments, heavy rain, and sea operations. These applications require special IP considerations, such as air and watertight designs without vents in the package. Thermal management remains a critical challenge for these PES units, especially for key components like inverters and battery packages, which are highly susceptible to overheating.

This study investigated the integration of heat pipe-based cooling systems with heatsinks as a thermal management solution. A 1 kW PES design was developed and analysed as a case study under varying ambient temperatures ranging from 10 °C to 50 °C and different power delivery scenarios. Both free and forced convection cooling methods were evaluated through experiments and validated simulations. The findings from this study demonstrated the effectiveness of heat pipe cooling systems in enhancing thermal performance, particularly when external cooling was applied using forced convection. This approach ensures the reliability and compactness of PES designs, making them suitable for diverse and demanding applications.

Key insights from the study include:

- Effectiveness of heat pipes: Heat pipe cooling systems successfully maintained operational temperatures for key PES components. Under free convection at an ambient temperature of 23 °C, the MOSFETs remained below 70 °C, and the LIBs stayed at 60 °C. Adding external 1.4 W fans for each heatsink achieved an additional 33 % temperature reduction in both MOSFETs and LIBs.
- *Performance under higher ambient temperatures:*
  (i) For ambient temperatures up to 43 °C, the MOSFETs remained below the acceptable threshold of 90 °C without requiring power reduction.
  (ii) At an ambient temperature of 50 °C, MOSFETs reached 96 °C under 1 kW power delivery. Reducing power delivery by 15 % brought the temperature back under 90 °C.
  (iii) Similarly, at 50 °C, the LIBs reached 87 °C under 1 kW power delivery. Reducing the power delivery to 0.7 kW and 0.5 kW lowered the LIB temperatures to 77 °C and 70 °C, respectively. At 40 °C, the LIBs remained below the critical 60 °C threshold with 0.5 kW power delivery.
- *Forced convection efficiency:* Using external 1.4 W fans for heatsinks resulted in an additional temperature reduction of 25–45 %, depending on ambient conditions. The highest cooling efficiency was observed at lower ambient temperatures. In the most critical scenario (1 kW power delivery at 50 °C ambient temperature), the MOSFETs reached a maximum temperature of 70 °C, while the LIBs remained below 60 °C for ambient temperatures up to 45 °C. However, at 50 °C ambient temperature and 0.7 kW power delivery, the LIBs slightly exceeded the critical threshold, reaching 61 °C.

Package price offers a practical and scalable approach due to its enhanced sealing capability and improved reliability. The validated simulation and experimental outcomes provide a strong foundation for transitioning this concept from laboratory testing to real-world application. Future work should focus on developing and evaluating airtight prototype units based on this design, including systematic testing of heatsink and heat pipe configurations with varying dimensions and orientations—such as vertical positioning of heatsinks for potentially higher cooling performance. Moreover, exploring advanced thermal technologies such as vapor chambers is recommended to further enhance performance in such compact and sealed electronic systems.

CRediT authorship contribution statement

Alireza E. Majd: Writing – review & editing, Writing – original draft, Visualization, Validation, Software, Methodology, Investigation, Formal analysis, Data curation, Conceptualization. **Collins E. Obazee:** Investigation, Formal analysis. **David S. Adebayo:** Writing – review & editing, Visualization, Supervision. **Armin R. Darvazi:** Writing – review & editing, Conceptualization. **Nduka N. Ekere:** Supervision, Conceptualization. **Fideline Tchuenbou-Magaia:** Writing – review & editing, Visualization, Supervision, Resources, Project administration, Funding acquisition. **Jin Wang:** Writing – review & editing, Supervision, Resources, Project administration.

Declaration of competing interest

The authors declare the following financial interests/personal relationships which may be considered as potential competing interests: Fideline Tchuenbou-Magaia reports financial support was provided by Innovate UK. Fideline Tchuenbou-Magaia reports financial support was provided by Horizon Europe. Fideline Tchuenbou-Magaia reports financial support was provided by University of Wolverhampton. This work was partially supported by the INNOVATE UK project No: 833831 and the EU Horizon 2020 Research, Innovation and Staff Exchange, ReACTIVE Too project No. 871163. The authors express their gratitude to the School of Engineering, Computing and Mathematical Sciences, University of Wolverhampton, for their invaluable support in facilitating the experimental tests for this study. Additionally, they extend their sincere thanks to the School of Engineering, Liverpool John Moores University, for providing the resources and support necessary to conduct the simulations. If there are other authors, they declare that they have no known competing financial interests or personal relationships that could have appeared to influence the work reported in this paper. If there are other authors, they declare that they have no known competing financial interests or personal relationships that could have appeared to influence the work reported in this paper.

Acknowledgments

This work was partially supported by the INNOVATE UK project No: 833831 and the EU Horizon 2020 Research, Innovation and Staff Exchange, ReACTIVE Too project No. 871163). The authors express their gratitude to the School of Engineering, Computing and Mathematical Sciences, University of Wolverhampton, for their invaluable support in facilitating the experimental tests for this study. Additionally, they extend their sincere thanks to the School of Engineering, Liverpool John Moores University, for providing the resources and support necessary to conduct the simulations.

Data availability

Data will be made available on request.

References

[1] L. Bodenes, R. Naturel, H. Martinez, R. Dedryvère, M. Menetrier, L. Croguennec, J. P. Pérès, C. Tessier, F. Fischer, Lithium secondary batteries working at very high temperature: capacity fade and understanding of aging mechanisms, J. Power Sources 236 (2013) 265–275, https://doi.org/10.1016/J.JPOWSOUR.2013.02.067.

[2] C. Liu, C. Zhang, H. Fu, X. Nan, G. Cao, Exploiting high-performance anode through tuning the character of chemical bonds for Li-ion batteries and capacitors, Adv. Energy Mater. 7 (1) (2017) 1601127, https://doi.org/10.1002/aenm.201601127.

[3] Y. Jin, Z. Zhao, S. Miao, Q. Wang, L. Sun, H. Lu, Explosion hazards study of grid-scale lithium-ion battery energy storage station, J. Energy Storage 42 (2021) 102987, https://doi.org/10.1016/J.EST.2021.102987.

[4] N.D. Williard, W. He, M.D. Osterman, M.G. Pecht, Reliability and failure analysis of Lithium ion batteries for electronic systems, in: 2012 13th International Conference on Electronic Packaging Technology & High Density Packaging, 2012, pp. 1051–1055, https://doi.org/10.1109/ICEPT-HDP.2012.6474788.

[5] X. Wu, K. Song, X. Zhang, N. Hu, L. Li, W. Li, L. Zhang, H. Zhang, Safety issues in lithium ion batteries: materials and cell design, Front. Energy Res. 7 (2019), https://doi.org/10.3389/fenrg.2019.00065.

[6] A.A. Pesaran, Battery thermal models for hybrid vehicle simulations, J. Power Sources 110 (2) (2002) 377–382, https://doi.org/10.1016/S0378-7753(02)00200-8.

[7] T. Waldmann, B.I. Hogg, M. Wohlfahrt-Mehrens, Li plating as unwanted side reaction in commercial Li-ion cells – a review, J. Power Sources 384 (2018) 107–124, https://doi.org/10.1016/J.JPOWSOUR.2018.02.063.

[8] J. He, R. Youssef, M.S. Hosen, M. Akbarzadeh, J. Van Mierlo, M. Berecibar, A novel methodology to determine the specific heat capacity of lithium-ion batteries, J. Power Sources 520 (2022) 230869, https://doi.org/10.1016/J.JPOWSOUR.2021.230869.

[9] D. Karimi, H. Behi, J. Jaguemont, M. El Baghdadi, J. Van Mierlo, O. Hegazy, Thermal concept design of MOSFET power modules in inverter subsystems for electric vehicles, in: 2019 9th International Conference on Power and Energy

Systems (ICPES), 2019, pp. 1–6, https://doi.org/10.1109/ICPES47639.2019.9105437.

[10] D. Reay, P. Kew, R. McGlen, Heat Pipes: Theory, Design and Applications, 6th ed., Butterworth-Heinemann, 2014.

[11] M.B.H. Mantelli, Thermosyphons and Heat Pipes: Theory and Applications, Springer, Cham, 2020.

[12] W. Srimuang, P. Amatachaya, A review of the applications of heat pipe heat exchangers for heat recovery, Renew. Sustain. Energy Rev. 16 (6) (2012) 4303–4315, https://doi.org/10.1016/J.RSER.2012.03.030.

[13] J. Smith, R. Singh, M. Hinterberger, M. Mochizuki, Battery thermal management system for electric vehicle using heat pipes, Int. J. Therm. Sci. 134 (2018) 517–529, https://doi.org/10.1016/J.IJTHERMALSCI.2018.08.022.

[14] N. Putra, B. Ariantara, R.A. Pamungkas, Experimental investigation on performance of lithium-ion battery thermal management system using flat plate loop heat pipe for electric vehicle application, Appl. Therm. Eng. 99 (2016) 784–789, https://doi.org/10.1016/J.APPLTHERMALENG.2016.01.123.

[15] B.I. Basok, Y.E. Nikolaenko, R.S. Melnyk, Thermal management of electronic devices using heat pipes, in: Yuwen Zhang (Ed.), Heat Pipes: Design, Application, and Technology, Nova Science Publisher, Inc., 2018, pp. 203–253 (ISBN 978-153613909-9.).

[16] V.I. Kornaga, D.V. Pekur, Yu.V. Kolomzarov, V.P. Kostylyov, V.M. Sorokin, R. M. Korkishko, Yu.E. Nikolaenko, Intelligence system for monitoring and governing the energy efficiency of solar panels to power LED luminaires, Semicond. Phys. Quantum Electron. Optoelectron. 24 (02) (2021) 200–209, https://doi.org/10.15407/spqeo24.02.200.

[17] A. Eslami Majd, F. Tchuenbou-Magaia, A.M. Meless, D.S. Adebayo, N.N. Ekere, A review on cooling systems for portable energy storage units, Energies 16 (18) (2023) 6525, https://doi.org/10.3390/en16186525.

[18] Z. Chen, Y. Yao, M. Danilovic, D. Boroyevich, Performance evaluation of SiC power MOSFETs for high-temperature applications, in: 2012 15th International Power Electronics and Motion Control Conference (EPE/PEMC), 2012, pp. DS1a.8-1–DS1a.8-9, https://doi.org/10.1109/EPEPEMC.2012.6397198.

[19] S. Pyo, K. Sheng, Junction temperature dynamics of power MOSFET and SiC diode, in: 2009 IEEE 6th International Power Electronics and Motion Control Conference, 2009, pp. 269–273, https://doi.org/10.1109/IPEMC.2009.5157397.

[20] Farnell, AMEC THERMASOL MHP-2550A300A. https://uk.farnell.com/amec-thermasol/mhp-2550a300a/heat-pipe-flat-300mmx50mmx2-5mm/dp/3972217?MER=BR-MER-MA-RECO-PDP-STM72143, 2024.

[21] Testo, Testo 883-1 Thermal Imager (Model 0560 8830). https://www.testo.com/en-UK/testo-883-1/p/0560-8830, 2025.

[22] A.B. Solomon, M. Sekar, S.H. Yang, Analytical expression for thermal conductivity of heat pipe, Appl. Therm. Eng. 100 (2016) 462–467, https://doi.org/10.1016/j.applthermaleng.2016.02.042.

[23] ANSYS Inc, ANSYS 2024 User Guide: Thermal Transient Analysis, ANSYS Inc., 2024. https://www.ansys.com/.

[24] Frank P. Incropera, David P. DeWitt, Theodore L. Bergman, Adrienne S. Lavine, Fundamentals of Heat and Mass Transfer, 6th ed., John Wiley & Sons, 2007.

[25] R. Gerhardt, Properties and Applications of Silicon Carbide, IntechOpen, 2011, https://doi.org/10.5772/615.

[26] A. Castellazzi, A. Fayyaz, G. Romano, L. Yang, M. Riccio, A. Irace, SiC power MOSFETs performance, robustness and technology maturity, Microelectron. Reliab. 58 (2016) 164–176, https://doi.org/10.1016/j.microrel.2015.12.034.

[27] J. Wang, M. Yang, K. Lu, Ventilation condition effects on heat dissipation of the lithium-ion battery energy storage cabin fire, Case Stud. Therm. Eng. 63 (2024) 105373, https://doi.org/10.1016/j.csite.2024.105373.

[28] F. Yao, X. Guan, M. Yang, C. Wen, Study on liquid cooling heat dissipation of Li-ion battery pack based on bionic cobweb channel, J. Energy Storage 68 (2023) 107588, https://doi.org/10.1016/J.EST.2023.107588.

[29] A. Belgibayeva, A. Rakhmetova, M. Rakhatkyzy, M. Kairova, I. Mukushev, N. Issatayev, G. Kalimuldina, A. Nurpeissova, Y.K. Sun, Z. Bakenov, Lithium-ion batteries for low-temperature applications: limiting factors and solutions, J. Power Sources 557 (2023) 232550, https://doi.org/10.1016/J.JPOWSOUR.2022.232550.

[30] S. Hemavathi, C.R. Jeevandoss, S. Srinivas, A.S. Prakash, Experimental studies on Li-ion battery pack for temperature distribution analysis during fast discharging and various ambient temperature conditions, Heat Transf. Res. 55 (2) (2024) 41–54, https://doi.org/10.1615/HeatTransRes.2023048880.

[31] J. Hou, M. Yang, D. Wang, J. Zhang, Fundamentals and challenges of lithium ion batteries at temperatures between −40 and 60 °C, Adv. Energy Mater. 10 (18) (2020), https://doi.org/10.1002/aenm.201904152.

[32] O.-J. Kim, Y.-H. Cho, J.-J. Kang, Y.-S. Yu, C. Kim, G.-Y. Yun, Exploration about the electrolyte system of Li-ion batteries for the wide temperature range operation, Electron. Mater. Lett. (2024), https://doi.org/10.1007/s13391-024-00488-x.

[33] K. Tikhonov, V.R. Koch, Li-ion Battery Electrolytes Designed for a Wide Temperature Range, 2006, https://doi.org/10.21236/ADA507154.

[34] J. Wang, Q. Zheng, M. Fang, S. Ko, Y. Yamada, A. Yamada, Concentrated electrolytes widen the operating temperature range of lithium-ion batteries, Adv. Sci. 8 (18) (2021), https://doi.org/10.1002/advs.202101646.